

Magnetic field-induced helical mode and topological transitions in a topological insulator nanoribbon

Luis A. Jauregui^{1,2}, Michael T. Pettes^{3†}, Leonid P. Rokhinson^{1,2,4}, Li Shi^{3,5} and Yong P. Chen^{1,2,4*}

The spin-helical Dirac fermion topological surface states in a topological insulator nanowire or nanoribbon promise novel topological devices and exotic physics such as Majorana fermions. Here, we report local and non-local transport measurements in Bi₂Te₃ topological insulator nanoribbons that exhibit quasi-ballistic transport over ~2 μm. The conductance versus axial magnetic flux Φ exhibits Aharonov-Bohm oscillations with maxima occurring alternately at half-integer or integer flux quanta ($\Phi_0 = h/e$, where h is Planck's constant and e is the electron charge) depending periodically on the gate-tuned Fermi wavevector (k_F) with period $2\pi/C$ (where C is the nanoribbon circumference). The conductance versus gate voltage also exhibits k_F -periodic oscillations, anti-correlated between $\Phi = 0$ and $\Phi_0/2$. These oscillations enable us to probe the Bi₂Te₃ band structure, and are consistent with the circumferentially quantized topological surface states forming a series of one-dimensional subbands, which undergo periodic magnetic field-induced topological transitions with the disappearance/appearance of the gapless Dirac point with a one-dimensional spin helical mode.

Three-dimensional topological insulators (TIs) are a new class of quantum matter with an insulating bulk and conducting surface states, topologically protected against time-reversal-invariant perturbations (such as scattering by non-magnetic impurities, crystalline defects and surface roughness)^{1,2}. The metallic surface states of TIs have been unambiguously demonstrated by surface-sensitive experiments, for example using angle-resolved photoemission spectroscopy (ARPES)^{3,4} and scanning tunnelling microscopy⁵. However, probing the surface states of TI bulk crystals (such as Bi₂Te₃; for a schematic of its bandstructure see Fig. 1a, where the bulk bands and the topological surface states, TSSs, are depicted) by transport measurements has been more challenging because of non-insulating bulk conduction⁶. Different approaches have been used to reduce the bulk contribution, such as by the fabrication of nanostructured devices based on nanowires/nanoribbons^{7–11} and ultrathin films^{12,13}.

Topological insulator nanowires (TINWs, including the nanoribbons (TINRs) studied here) are topologically analogous to hollow metallic cylinders. Confinement of the surface along the circumference (C) gives discretely quantized circumferential momentum k_{\perp} (Fig. 1b) and generates a series of one-dimensional surface subbands or quantized surface-state modes. Unique to TINWs, the spin-helical surface states cause the spin to be tangential to the surface and perpendicularly locked to the momentum, such that a particle (with momentum along the transport axial direction, k_{\parallel}), as depicted in Fig. 1b for a TINR) picks up a Berry's phase of π due to the 2π rotation of the spin as it travels around the circumference. When an axial magnetic field B is applied (with flux $\Phi = BA$, where A is the cross-sectional area), the electron wavefunction picks up an Aharonov–Bohm (AB) phase of $2\pi\Phi/\Phi_0$ around the circumference (with flux quanta $\Phi_0 = h/e$, where h is

Planck's constant and e is the electron charge). Considering both of these effects (the Berry's phase and the AB phase), the one-dimensional subbands^{14–19} have the following Φ -dependent dispersion (depicted in Fig. 1c):

$$E_l(k_{\parallel}) = \pm \hbar v_F \sqrt{k_{\parallel}^2 + k_{\perp}^2},$$
$$\text{with quantized } k_{\perp} = \Delta k \left(l + 0.5 - \frac{\Phi}{\Phi_0} \right) \quad (1)$$

where \hbar is the reduced Planck's constant, v_F is the TSS Fermi velocity, $\Delta k = 2\pi/C$ and l ($0, \pm 1, \pm 2, \dots$) is the angular momentum quantum number.

Two particularly interesting cases occur: (1) when Φ is an even multiple of $\Phi_0/2$ (including $\Phi = 0$), the Dirac point of TSS is gapped (due to the Berry's phase, responsible for the 0.5-shift in equation (1) for k_{\perp}) and all subbands are doubly degenerate (with two opposite choices of k_{\perp}); (2) when Φ is an odd multiple of $\Phi_0/2$, the gap re-closes due to the AB phase cancelling (modulo 2π) the Berry's phase, and a spinless (non-degenerate, $k_{\perp} = 0$) zero-gap one-dimensional mode^{14–19} emerges from the restored Dirac point (DP) (other subbands with non-zero k_{\perp} remain gapped and doubly degenerate). An axial Φ through the core therefore drives periodic topological transitions in the surface subbands, changing from all being doubly degenerate with a gapped DP at integer Φ_0 (including zero) to containing a topologically protected, non-degenerate one-dimensional spin helical mode with restored DP at half-integer Φ_0 . This one-dimensional spin helical mode^{20,21} is unique to TINWs (it is absent in carbon nanotubes, for example) and is predicted to be topologically protected (forbidding the one-dimensional

¹Birck Nanotechnology Center, Purdue University, West Lafayette, Indiana 47907, USA. ²School of Electrical and Computer Engineering, Purdue University, West Lafayette, Indiana 47907, USA. ³Department of Mechanical Engineering, University of Texas at Austin, Austin, Texas 78712, USA. ⁴Department of Physics and Astronomy, Purdue University, West Lafayette, Indiana 47907, USA. ⁵Materials Science and Engineering Program, University of Texas at Austin, Austin, Texas 78712, USA. [†]Present address: Department of Mechanical Engineering, University of Connecticut, Storrs, Connecticut 06269, USA.

*e-mail: yongchen@purdue.edu

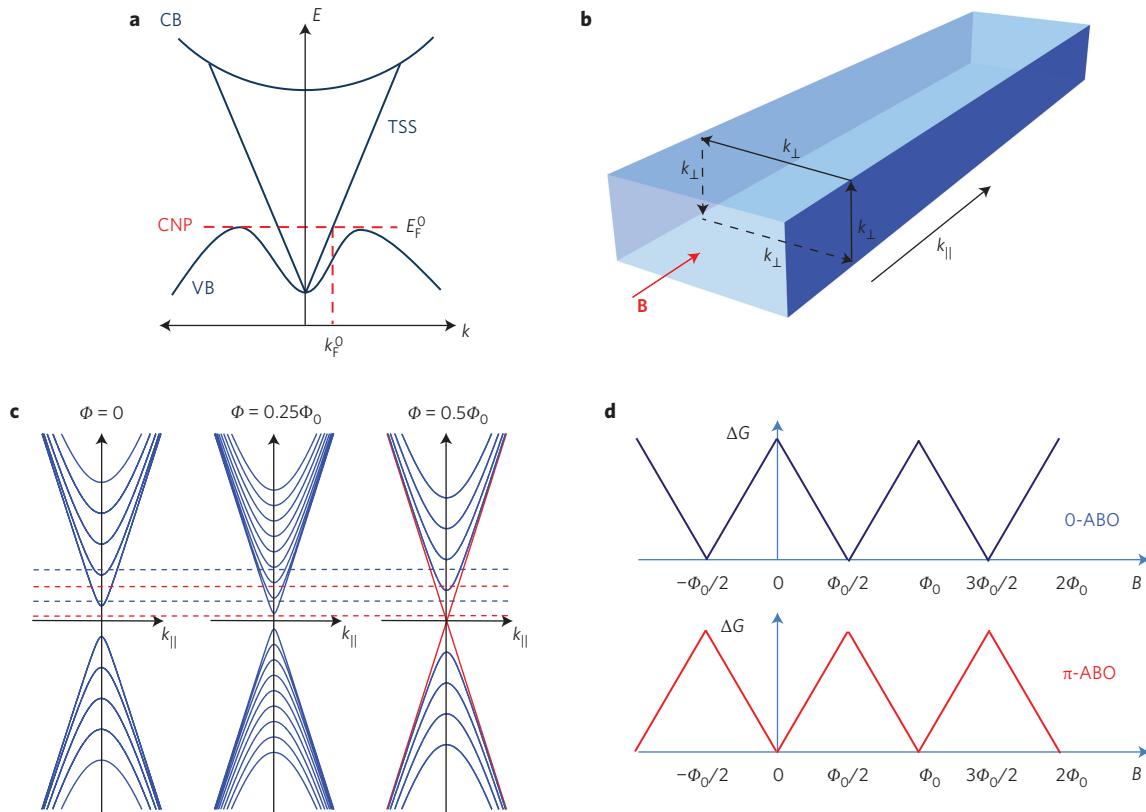


Figure 1 | Schematics of the Bi_2Te_3 bandstructure, surface state modes and expected magnetoconductance oscillation patterns in TINRs. **a**, Schematic band diagram of bulk Bi_2Te_3 . The bulk conduction band (CB), topological surface states (TSSs) and bulk valence band (VB) are labelled. Note that the DP is buried inside the VB, so only n-type TSSs are accessible inside the bulk bandgap. Horizontal and vertical dashed lines mark the minimum Fermi energy (E_F^0 , at top of VB) and momentum (k_F^0) to observe surface-state conduction (conduction by the bulk valence band states would dominate for lower E_F or k_F). The charge neutrality point (CNP) also occurs close to E_F^0 . **b**, Schematic of a TINR, where k_{\parallel} and k_{\perp} indicate the TSS momentum parallel and perpendicular to the TINR axis. The applied axial magnetic field B is depicted by a red arrow. **c**, Schematic of the (circumferentially quantized) TINR surface-state modes or surface subbands (neglecting bulk bands) depicted for three representative axial magnetic fluxes (Φ , in units of magnetic flux quanta $\Phi_0 = h/e$) through the NR cross-section. For each Φ , multiple surface-state modes (subbands) arise from discretely quantized k_{\perp} (equation (1)). **d**, Schematic of the expected magnetoconductance ($\Delta G(B)$) oscillation pattern at two different types of E_F position (exemplified by the blue and red dashed horizontal lines in **c**), giving rise to 0-ABO and π -ABO, respectively.

backscattering that reverses k_{\parallel}) and to host Majorana fermions when proximity-coupled to ordinary s -wave superconductors^{15,16,22,23}. In both cases, the adjacent subbands (quantized surface modes) are separated by an energy gap (measured at $k_{\parallel} = 0$) of $\Delta E = \hbar v_F \Delta k$ (see also the schematic Fermi surface presented in Supplementary Fig. 1). As depicted in Fig. 1c,d for ballistic TINWs with the Fermi energy (E_F) near the Dirac point (up to $|E_F| < \Delta E/2$), the conductance G versus Φ is dominated by the presence or absence of the helical mode. Therefore, G versus Φ (or B) should oscillate with period Φ_0 and should reach maxima at odd multiples of $\Phi_0/2$, known as Aharonov–Bohm oscillations with a phase of π (π -ABO)^{14,18}. However, if $\Delta E/2 < E_F < \Delta E$, for $\Phi = \text{even multiples of } \Phi_0/2$ there is a doubly degenerate surface mode, while for $\Phi = \text{odd multiples of } \Phi_0/2$ there is only a single helical mode. G versus Φ therefore oscillates with period Φ_0 and has maxima at even multiples of $\Phi_0/2$, known as Aharonov–Bohm oscillations with zero phase (0-ABO). If $\Delta E < E_F < 3\Delta E/2$, G versus Φ should exhibit π -ABO again, and so on. Such alternations between π -ABO and 0-ABO would occur periodically in E_F , with period ΔE (Fig. 1c,d)^{14,15}. A schematic of the expected $\Delta G(B)$ (after subtracting an E_F -dependent background in $G(B)$) for different values of E_F is presented in Fig. 1d. Previously, ABOs with a period of Φ_0 and $G(B)$ maxima at even multiples of $\Phi_0/2$ (0-ABO) have been measured in TINRs^{7,8,10}, and the phase (0) of these ABOs was insensitive to gate voltage⁸ V_g . Theories have suggested¹⁴ disorder, which broadens the surface subbands and makes the number of modes

for even or odd multiples of $\Phi_0/2$ unidentifiable, as the reason for the ABO phase not being dependent on V_g .

Here, we demonstrate gate-tunable ABOs with k_F -periodic phase alternation between 0 and π in quasi-ballistic Bi_2Te_3 nanoribbon field-effect devices. The conductance versus gate voltage at $\Phi = 0$ and $\Phi_0/2$ also exhibits clear, but anti-correlated k_F -periodic oscillations, which enable us to extract the minimal Fermi energy and momentum for TSSs to dominate over the contribution of the bulk valence band (BVB). These magnetic and gate-dependent conductance oscillations are consistent with the circumferentially quantized TSSs forming a series of one-dimensional subbands, which undergo periodic magnetic field-induced topological transitions with opening/closing of the Dirac gap, accompanied by the disappearance/appearance of the one-dimensional spin helical mode.

Samples and field effect

We synthesized single-crystal Bi_2Te_3 nanoribbons using a catalyst-free vapour–solid method as described previously²⁴ and transferred them to 500- μm -thick SrTiO_3 (STO) substrates as the dielectric for back gating^{13,24,25}. We have previously shown that our Bi_2Te_3 nanoribbons can be tuned into the bulk-insulating, topological transport regime²⁴. All the data presented in the following were measured in a representative device with a nanoribbon width of 150 nm and thickness of 60 nm, as measured by atomic force microscopy. Figure 2a shows a scanning electron microscope (SEM) image of this device

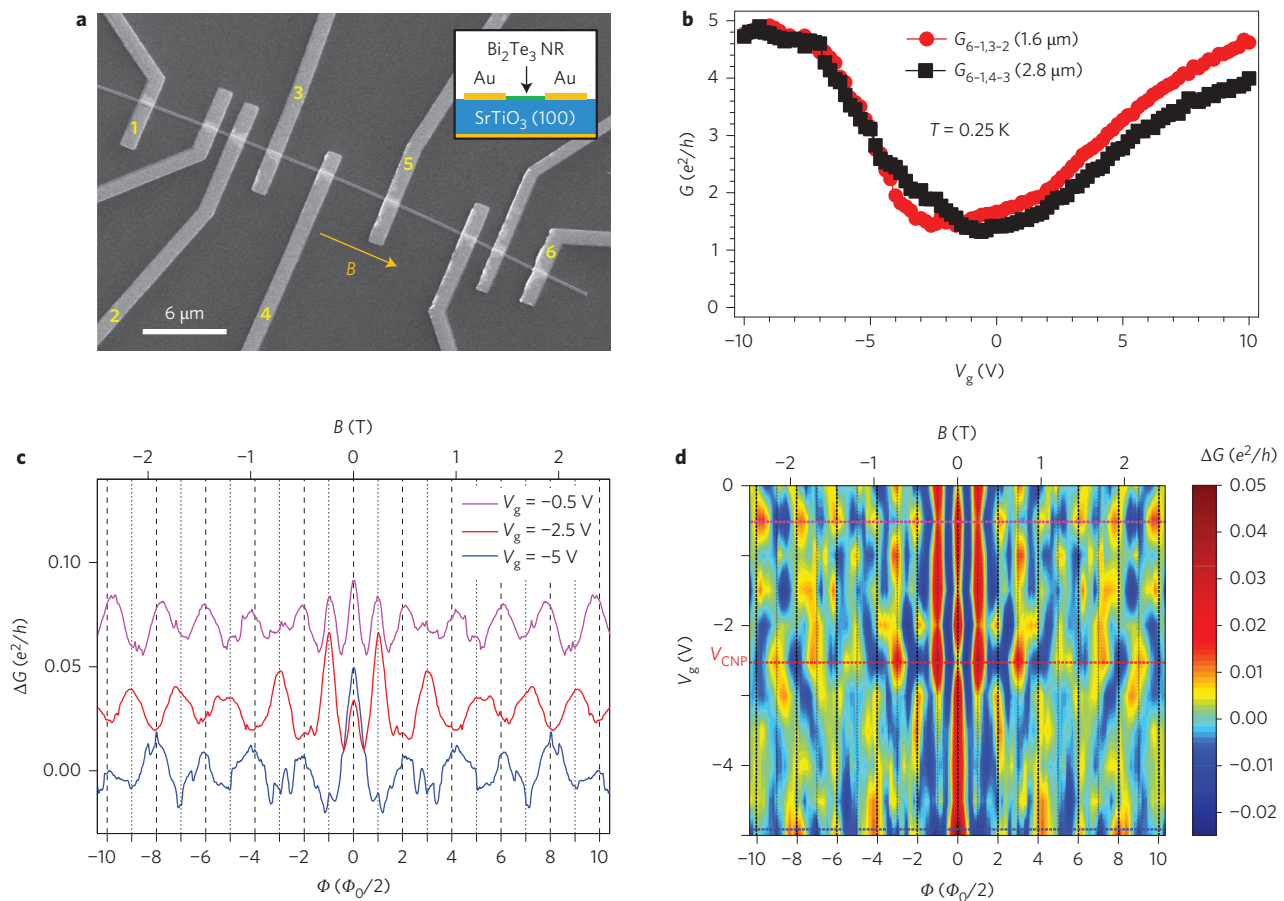


Figure 2 | Ambipolar field effect, demonstrating quasi-ballistic conduction and gate-tunable 0- and π -ABOs, demonstrating TSS modes in TINRs.

a, Scanning electron microscope image of a 150-nm-wide, 60-nm-thick TINR multi-terminal device on an STO substrate studied in this work. The orange arrow indicates the direction of the applied B field. Inset: schematic of the device cross-section. **b**, Four-terminal conductance G versus back-gate voltage V_g , measured for two different segments of the TINR (between voltage probes 3 and 2, with length 1.6 μm , and between 4 and 3, with length 2.8 μm). Current $I = 1$ nA is applied between electrodes 6 and 1 (ground). **c**, Magnetoconductance ($\Delta G(B)$, with a smooth background subtracted) in units of e^2/h versus B field (top axis, with corresponding magnetic flux Φ in units of half-flux-quantum ($\Phi_0/2 = h/2e$) on the bottom axis) at different V_g . Curves are offset vertically for clarity. **d**, Colour plot of ΔG (in units of e^2/h) versus V_g (in 0.5 V steps) and B . The horizontal colour-coded dashed lines correspond to the same colour-coded ΔG in **c**. Vertical dashed/dotted lines in **c** and **d** mark integer/half-integer flux quanta (even/odd multiples of $\Phi_0/2$). Data in **b–d** were measured at $T = 0.25$ K. The conductance in **c** and **d**, as well as in Figs 3 and 4, was measured between electrodes 3 and 2. Magnetoconductance data in Figs 2 and 3 have been symmetrized between opposite B -field directions.

with a schematic of its cross-section shown in the inset. Qualitatively similar data have been measured in several other devices.

Figure 2b shows the ambipolar field effect in four-probe conductance G measured with current $I = 1$ nA at $T = 0.25$ K for different segments of the TINR depicted in Fig. 2a. Here, $G_{i-j,k-l}$ denotes the four-probe conductance measured with current leads (i,j) and voltage probes (k,l). By varying V_g , carriers are tuned from p-type to n-type, with a minimum of G for $V_g \approx -2.5$ V (V_{CNP} , the charge neutrality point). The measured G versus V_g for two segments of the TINR, with different channel lengths $L_{\text{ch}} = 1.6$ and 2.8 μm for $G_{6-1,3-2}$ and $G_{6-1,4-3}$, respectively, are similar in magnitude, suggesting a quasi-ballistic transport.

Aharonov–Bohm and gate-dependent oscillations

Figure 2c depicts the low-temperature ($T = 0.26$ K) magnetoconductance ($\Delta G(B) = G(B) - f(B)$, where $f(B)$ is a smooth background subtracted from the raw data $G(B)$) versus the B field (depicted in Fig. 2a as an orange arrow) parallel to the nanoribbon axis, at three representative values of V_g . $\Delta G(B)$ oscillates periodically with B , with a period $\Delta B = 0.48$ T for all V_g . The measured ΔB agrees with the expected period for an ABO of $\Phi_0/A = 0.48$ T

(where $A \approx 9,000$ nm² is the measured TINR cross-sectional area). At $V_g = -5$ V $< V_{\text{CNP}}$ ($E_F < E_F^0$, inside the bulk valence band, where E_F^0 is the energy of the top of the bulk valence band), we observe $\Delta G(B)$ maxima at even multiples of $\Phi_0/2$ (integer flux quanta) and minima at odd multiple of $\Phi_0/2$, as previously observed (0-ABO)^{7,8}. We have not observed π -ABO for $V_g < V_{\text{CNP}}$, possibly due to the strong contribution from the bulk valence band, which is expected to dominate the conduction for $E_F < E_F^0$ as depicted in the band structure of Bi_2Te_3 (Fig. 1a). As we increase V_g and thus raise E_F into the TSS, another type of ABO becomes observable. For example, for $V_g \sim V_{\text{CNP}} \approx -2.5$ V ($E_F \sim E_F^0$), we observe ABO with $\Delta G(B)$ maxima at odd multiples of $\Phi_0/2$ (half-integer flux quanta) and minima at even multiples of $\Phi_0/2$ (except at $\Phi = 0$), in agreement with the predicted π -ABO (see Supplementary Fig. 6, for an explanation of how we distinguish between π -ABO, 0-ABO and the Altshuler–Aronov–Spivak oscillations (AAS)). The small peak at $B = 0$ can be attributed to weak anti-localization^{9,24,26–28} (WAL), which probably also occurs and contributes to the peak at $B = 0$ observed for other values of V_g . At $V_g = -0.5$ V, we observe ΔG peaks primarily at even multiples of $\Phi_0/2$, but also a few peaks (especially at $\Phi_0/2$) at odd

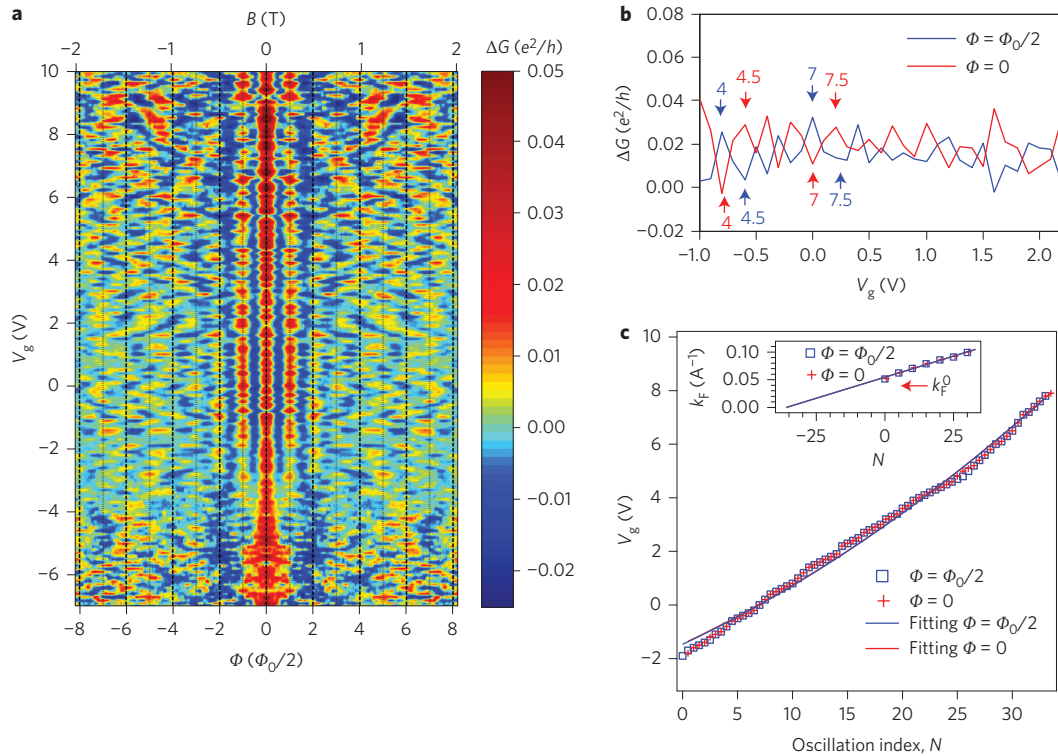


Figure 3 | Analysis of quantized TSS subbands in gate-dependent conductance oscillations and 0- and π -ABO alternations. **a**, Colour plot of ΔG versus V_g and Φ . Vertical dashed lines represent integer flux quanta ($\Phi =$ even multiples of $\Phi_0/2$), and vertical dotted lines represent half-integer flux quanta ($\Phi =$ odd multiples of $\Phi_0/2$). A zoomed-in view is shown in Supplementary Fig. 2. **b**, ΔG versus V_g for $\Phi = 0$ and $\Phi_0/2$, plotted from the corresponding vertical cuts in **a**. Peaks/dips (dips/peaks) in the $\Delta G(V_g)$ curve at $\Phi = \Phi_0/2$ ($\Phi = 0$) are assigned numbers (see text for details) starting from $N = 0$ at $V_g = V_0 = -1.9$ V (top of the BVB). **c**, V_g of the ΔG peaks/dips versus N for $\Phi = 0$ and $\Phi_0/2$. Solid curves are fittings of V_g versus N using equation (2). Inset: extracted Fermi momentum (k_F) versus N for $\Phi = 0$ and $\Phi_0/2$ (only selected data points with N in increments of five are shown for clarity). The solid line is a linear fit. The extracted k_F for $N = 0$ ($k_F^0 \approx 0.05 \text{ \AA}^{-1}$) is in reasonable agreement with the minimal momentum (depicted in Fig. 1a) for TSS to appear above the top of the BVB measured by ARPES⁴ in Bi_2Te_3 . $T = 0.25$ K for all measurements in **a-c**.

multiples of $\Phi_0/2$, suggesting competition between 0-ABO (more dominant at this V_g) and π -ABO.

Figure 2d presents a colour plot of ΔG versus the parallel B field and V_g at $T = 0.25$ K. For $-2.5 \text{ V} < V_g < 0 \text{ V}$ we observe that ΔG has maxima at alternate values of even or odd integers of $\Phi_0/2$. Such an alternation is particularly notable between the two more prominent peaks at $\Phi = 0$ and $\Phi = \Phi_0/2$. However, for $V_g < -2.5$ V (below CNP), the ΔG peak at $\Phi = \Phi_0/2$ vanishes, and the peak at $\Phi = 0$ becomes very prominent. The ΔG peak at $\Phi = \Phi_0/2$ is the first oscillation from the π -ABO and is the strongest as it may be less affected by the Zeeman energy than the higher odd multiples of $\Phi_0/2$ (which can be more easily de-phased at higher B field in spin-orbit-coupled systems^{29–31}). Also, this ΔG peak at $\Phi = \Phi_0/2$ (unique to TSS^{20,21}) vanishing for $V_g < V_{\text{CNP}} \approx -2.5$ V is consistent with the Bi_2Te_3 band structure⁴, where the DP of TSS is buried inside the BVB, and the BVB will dominate the conduction below the CNP (close to the top of the BVB).

Figure 3a presents a higher-resolution colour map of ΔG versus the parallel B field and V_g (B -field step = 4 mT, V_g step = 100 mV) for $-7 \text{ V} < V_g < +10 \text{ V}$ (see also Supplementary Fig. 2 for a zoomed-in view over a smaller range of B and V), where the gate-induced alternation between 0-ABO and π -ABO is again observed (for V_g down to $V_0 \approx -1.9$ V, slightly above V_{CNP} in this measurement). Figure 3b shows a plot of ΔG versus V_g (vertical cuts from Fig. 3a) for $\Phi = 0$ and $\Phi_0/2$ plotted over a relatively small V_g range for clarity. Both $\Delta G(V_g)$ curves exhibit clear oscillations, but the two sets of oscillations are $\sim 180^\circ$ out of phase, where the maxima (minima) in one curve tend to occur at the minima (maxima) of the other curve. We label each ΔG peak (dip) in the data measured at $\Phi = \Phi_0/2$ ($\Phi = 0$) with an integer oscillation index (N , increasing

with increasing V_g), starting with $N = 0$ (first ΔG peak (dip)) at $V_g = V_0$ (below V_0 , neither out-of-phase oscillations between the two $\Delta G(V_g)$ curves nor alternations between π -ABO and 0-ABO are evident), while we label each ΔG dip for $\Phi = \Phi_0/2$ (peak for $\Phi = 0$) as $N + 1/2$ (examples in Fig. 3b). For $V_g > V_0$ (note that V_0 is associated with the V_g required to reach the top of the BVB, labelled in Fig. 1a as E_F^0 , above which the surface-state conduction dominates), we can relate V_g with k_F of the TSS using

$$n_s = C_{\text{ox}}(V_g - V_0)/e = ((k_F)^2 - (k_F^0)^2)/4\pi \quad (2)$$

where n_s is the surface carrier density, C_{ox} is the STO capacitance and k_F^0 is the k_F at the top of the BVB (note that with a relatively large number of transverse k_\perp modes occupied in our samples for $V_g > V_0$, the standard results for two-dimensional spin-helical fermions can be used to relate the gate-induced TSS carrier density with k_F ; for more discussions see Supplementary Fig. 1). The observed V_g versus N can be well fitted (solid curves in Fig. 3c) to equation (2) (assuming $k_F = k_F^0 + N\Delta k$, where $\Delta k = 2\pi/C = 0.0015 \text{ \AA}^{-1}$ represents the quantized momentum encircling the TINR with $C = 420$ nm, the TINR circumference), from which we obtain $C_{\text{ox}} \approx 100 \text{ nF cm}^{-2}$ and $k_F^0 \approx 0.05 \text{ \AA}^{-1}$. We have also checked that the introduction of an uncertainty as large as ± 0.5 V in the choice of the $N = 0$ peak does not significantly change the extracted C_{ox} and k_F^0 . The extracted C_{ox} is within the range of the STO capacitance measured at low temperatures in other nanodevices^{13,24,33}. We plot the extracted $k_F = (4\pi C_{\text{ox}}/e(V_g - V_0) + (k_F^0)^2)^{1/2}$ versus N in the inset of Fig. 3c to demonstrate that the oscillations (indexed by N)

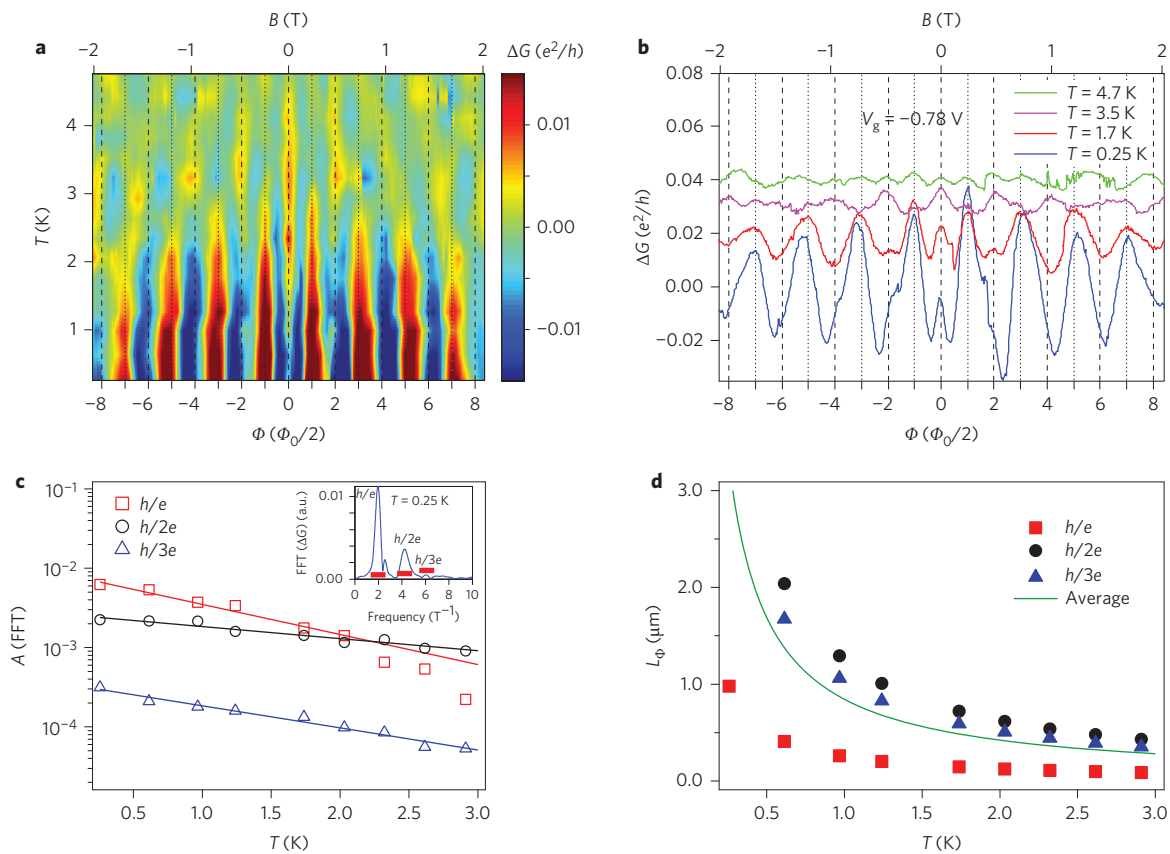


Figure 4 | Temperature dependence of the AB oscillations in TINRs, confirming quasi-ballistic transport. **a**, Colour plot of ΔG versus T and Φ for $V_g = -0.78$ V. **b**, ΔG versus Φ at different T . For **a** and **b**, vertical dashed lines represent $\Phi =$ even multiples of $\Phi_0/2$ (integer flux quanta), while dotted lines represent $\Phi =$ odd multiples of $\Phi_0/2$ (half-integer flux quanta). Traces are offset vertically for clarity. **c**, Temperature-dependent amplitude of the FFT ($A(\text{FFT})$, in log scale) corresponding to the h/e , $h/2e$ and $h/3e$ peaks (inset) at $V_g = -0.78$ V. Solid lines are exponential fits. Inset: fast Fourier transform (FFT) of ΔG versus B at $T = 0.25$ K. The peak amplitude is defined as the integrated area under the corresponding interval represented by the red horizontal line segment. **d**, Temperature dependence of the phase coherence length L_{ϕ} , extracted from FFT peaks. An average of the three data sets is shown as a solid line.

are periodic in k_F . The $k_F^0 \approx 0.05 \text{ \AA}^{-1}$ agrees with the minimum TSS momentum for the energy to exceed the top of the BVB (depicted in Fig. 1a), as measured by ARPES^{3,4} on bulk Bi_2Te_3 . For $k_F < k_F^0$, conduction is dominated by the BVB states and neither the π -ABO nor Δk -periodic $\Delta G (V_g)$ oscillations due to TSS subbands can be observed. Also, assuming a linear E_F versus k_F dispersion, we extract $E_F^0 = \hbar v_F k_F^0 \approx 133$ meV with $v_F = 4.1 \times 10^5 \text{ m s}^{-1}$, in excellent agreement with the ARPES-measured energy separation between the BVB top and the Dirac point, called E_3 in ref. 4. Therefore, the observed π -ABO and the gate-tunable phase (0 or π) in our TINRs are strong transport experimental evidence of the TSS and the formation of the one-dimensional helical mode in TINRs. The measured amplitudes of the four-terminal conductance (G of a few e^2/h) and of the ABO ($\Delta G < \sim 0.1 e^2/h$) are similar to previously reported values^{20,21}, and notably smaller than those expected for fully ballistic two-terminal conductance measured with transparent contacts ($G_2 \approx 40 e^2/h$ with $\Delta G_2 \approx 1 e^2/h$ for ~ 40 subbands in our samples, modulated by $+1/-1 e^2/h$ with the appearance/disappearance of the helical mode). It has been suggested that the measured amplitudes (G and ΔG) are not only dependent on subband occupation, but can also be strongly influenced by various other factors such as disorder (which can reduce these amplitudes)^{14,34} and invasive contacts^{32,35,36} (whose reflection and transmission coefficients enter the four-terminal G).

Quasi-ballistic transport from the temperature dependence
From previous studies in metallic and semiconducting rings³⁷, the T dependence of the ABO is known to exhibit different behaviour in diffusive and ballistic regimes. The amplitude of ABO in diffusive

TINRs shows a $\sim T^{-1/2}$ dependence^{7,8}, while in ballistic Bi_2Se_3 TINRs the amplitude has been found to decay exponentially¹⁰ with T . Figure 4a presents a colour plot of ΔG versus parallel B field for $0.25 \text{ K} < T < 5 \text{ K}$ at $V_g = -0.78$ V. We observe that the ABO amplitude decreases and the phase changes with increasing temperature. Figure 4b shows horizontal cuts (ΔG versus B) of Fig. 4a at a few representative values of T , where the change of phase is clearly observed (from π -ABO to 0 -ABO). For example, at $T = 0.25$ K, the π -ABO is dominant, while at $T \approx 3.5$ K the oscillations are 0 -ABO. On the other hand, for $V_g = -1.2$ V (Supplementary Fig. 3), 0 -ABOs are dominant at $T = 0.3$ K, while oscillations contain more π -ABOs (ΔG peaks mainly at odd multiples of $\Phi_0/2$) at $T \approx 2.3$ K. This change of phase with T may be related to a similar mechanism such as dephasing by disorder^{14,18}. To analyse the T dependence of ABOs, we computed the fast Fourier transform (FFT, the absolute value; an example for $T = 0.25$ K is shown in the inset of Fig. 4c) of the ΔG versus B data for different T . In the FFT we observe clear peaks at frequencies corresponding to periods h/e , $h/2e$ and $h/3e$ in the magnet flux. The n th harmonic of the fundamental period (h/e) is from electrons that travel around the circumference of the TINR n times³⁷. The probability of an electron enclosing the TINR circumference multiple times decreases with n , so the FFT amplitudes drop with increasing n . The T -dependent amplitudes, obtained by integration of h/e , $h/2e$ and $h/3e$ FFT peaks over intervals indicated by red horizontal lines in the inset of Fig. 4c, are plotted in Fig. 4c. These amplitudes are found to decrease exponentially with increasing temperature ($A(\text{FFT}) \sim e^{-b_n T}$), as previously reported for rings made from

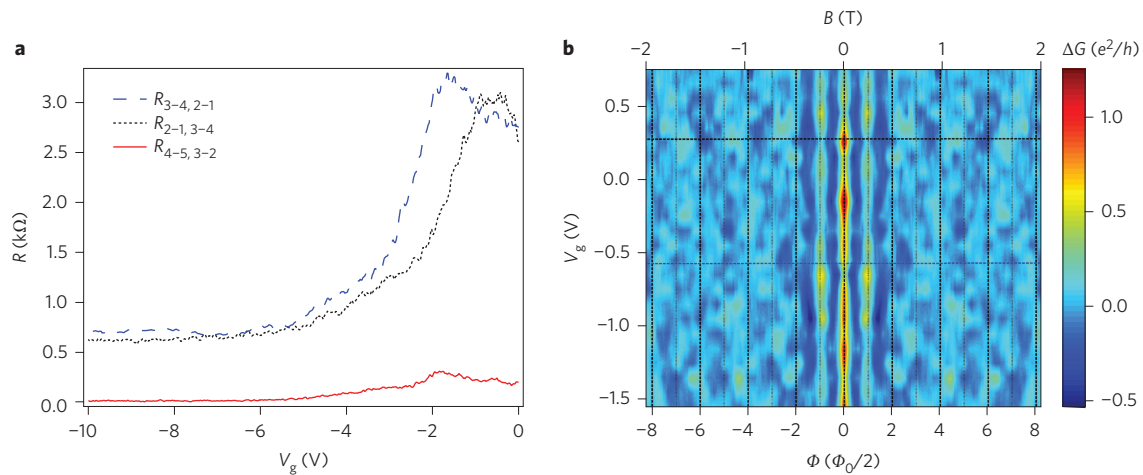


Figure 5 | Non-local transport in TINRs. Field-effect and gate-tunable magnetoconductance oscillations. **a**, Field effect of a non-local resistance R is measured with different sets of electrodes (that is, $R_{2-1,3-4}$ with current leads 2-1 and voltage probes 3-4, see device image in Fig. 2a). **b**, Colour plot of non-local $\Delta G_{2-1,3-4}$ versus V_g and Φ . Vertical dashed lines represent integer flux quanta and dotted lines half-integer flux quanta. Horizontal dashed dotted lines are cuts at two representative values of V_g (Supplementary Fig. 5). Data are measured at $T = 0.25$ K with $I = 1$ nA.

ballistic two-dimensional electron gases (2DEGs)³⁷ and TINRs¹⁰. While theories have predicted the decay rates $b_n = nC/(2TL_\phi)$, where L_ϕ is the phase coherence length, previous experiments in quasi-ballistic devices have shown that b_n is not always linearly dependent on n and the deviation was attributed to thermal averaging^{10,37}. In our devices, we found both types of behaviour, depending on the value of V_g (for example, b_n is not proportional to n at $V_g = -0.78$ V, but $b_n \propto n$ at $V_g = -1.2$ V, as shown in Supplementary Fig. 3). Hence, we calculate L_ϕ from each n th harmonic as $L_\phi = nC/(2Tb_n)$, shown in Fig. 4d, where the average L_ϕ is also plotted. The extracted L_ϕ for each n th harmonic of h/e (and their average) shows a similar T dependence ($L_\phi \approx T^{-1}$), with an average $L_\phi = 3 \mu\text{m}$ at $T \approx 0.25$ K. The same inverse T dependence was measured at $V_g = -1.2$ V (Supplementary Fig. 3). It is expected that in the ballistic regime³⁷, where fermions are weakly coupled to the environment, decoherence is dominated by fluctuations of the environment, resulting in an $L_\phi \sim T^{-1}$ dependence. In contrast, previous measurements on more disordered diffusive TINWs or NRs^{7,26-28} and 2DEG rings³⁸⁻⁴⁰ have shown an $L_\phi \sim T^{-a}$ dependence, with $a \approx 0.4-0.5$. Obtaining such large $L_\phi \approx 3 \mu\text{m}$ (comparable to or larger than the channel length) at low T and a distinctive exponential T dependence of the amplitude of ABOs (in contrast to previously studied more disordered and diffusive TINRs^{7,8,24}, where A (FFT) $\sim T^{-1/2}$) are strong signatures of quasi-ballistic transport in our TINRs. The measured $L_\phi \approx 3 \mu\text{m}$ at low T is also consistent with the fact that we can observe ABOs from $\Delta G_{6-1,4-3}$ with $L_{\text{ch}} \approx 3 \mu\text{m}$ (Supplementary Fig. 4).

Non-local AB oscillations

Previous experiments in 2DEG rings have shown that the ABO phase could be shifted with V_g when only one arm of the ring is gated (such asymmetric gating induces a potential difference between two arms)³⁶. Although the Onsager principle could cause only discrete phases (0 or π) to be seen in 'local' electrical measurements (as in our experiments, $G_{6-1,3-2}$ or $G_{6-1,4-3}$) under this scenario, when non-local electrical measurements were performed, a continuous change of ABO phase could be observed^{36,41,42}. We performed non-local electrical measurements in our TINRs (the device depicted in Fig. 2a). Figure 5a displays the non-local resistance $R_{2-1,3-4}$ and $R_{3-4,2-1}$ versus V_g at $T = 0.25$ K, where an ambipolar field effect is also observed, with significant values (~ 3 k Ω) of non-local resistances at CNP ($V_g \approx -2$ V). The two non-local resistances $R_{2-1,3-4}$ and $R_{3-4,2-1}$ are similar in magnitude, with a separation between the current and

voltage probes of $L_{\text{ch}} = L_{2-3} = 1.6 \mu\text{m}$. However, the non-local resistance $R_{4-5,3-2}$, with $L_{\text{ch}} = L_{3-4} = 2.8 \mu\text{m}$, is considerably reduced compared to $R_{2-1,3-4}$. Such a large reduction (by a factor of more than 10) of non-local resistance when L_{ch} is increased only by a factor of approximately two may be related to quasi-ballistic transport. Figure 5b presents a colour plot of non-local $\Delta G_{2-1,3-4}$ versus the parallel B field and V_g at $T = 0.25$ K (horizontal colour-coded dashed lines correspond to $\Delta G_{2-1,3-4}$ versus the parallel B field at representative values of V_g as shown in Supplementary Fig 5). The period of non-local ABO oscillations $\Delta B \approx 0.48$ T is consistent with the TINR cross-sectional area and the period observed in local measurements (Fig. 2). The amplitude of the ABO (ΔG) measured in the non-local configuration ($\sim 1 e^2/h$) is about one order of magnitude larger than that of the ABO measured in the local configuration ($\sim 0.1 e^2/h$), and is the largest ABO amplitude reported in TIs so far. A similar enhancement of the ABO amplitude was previously measured in 2DEG rings using a non-local configuration³⁶. Most importantly, at different values of V_g , only discrete ABO phases (0 or π only) are measured in our TINRs in the non-local configuration, contrary to a continuous change of the ABO phase measured in asymmetrically gated 2DEG rings. We can therefore rule out asymmetric gating as being responsible for the discrete change in the ABO phase (between 0 or π) at different V_g in our TINRs, as observed in both local and non-local configurations.

Conclusions

We have demonstrated quasi-ballistic transport in TINRs from the channel length (L_{ch})-insensitive conductance and field effect and the exponentially decaying T dependence of the ABO amplitude. In both local and non-local magnetoconductance measurements we observed π -ABOs and 0 -ABOs alternating periodically with k_F (tuned by V_g , with period $\Delta k = 2\pi/C$, where C is the nanoribbon circumference). The conductance oscillations in V_g (periodic in k_F and observed even at $B = 0$) reveal quantized surface-state modes. From the data we extracted the minimal k_F for the Fermi energy to cross only TSSs and found good agreement with ARPES results. These observations are consistent with a periodic modulation (and topological transitions) of surface subbands by an axial Φ through the TINR core, particularly the existence of the topologically protected one-dimensional helical mode for $\Phi = \text{odd multiple of } \Phi_0/2$. Such a helical mode in TINRs may be important for the development of topologically protected electronic or spintronic devices and for hosting Majorana fermions.

Received 20 February 2015; accepted 12 November 2015;
published online 18 January 2016

References

- Hasan, M. Z. & Kane, C. L. Colloquium: topological insulators. *Rev. Mod. Phys.* **82**, 3045–3067 (2010).
- Qi, X.-L. & Zhang, S.-C. Topological insulators and superconductors. *Rev. Mod. Phys.* **83**, 1057–1110 (2011).
- Hsieh, D. *et al.* A tunable topological insulator in the spin helical Dirac transport regime. *Nature* **460**, 1101–1105 (2009).
- Chen, Y. L. *et al.* Experimental realization of a three-dimensional topological insulator, Bi₂Te₃. *Science* **325**, 178–181 (2009).
- Zhang, T. *et al.* Experimental demonstration of topological surface states protected by time-reversal symmetry. *Phys. Rev. Lett.* **103**, 266803 (2009).
- Qu, D.-X., Hor, Y., Xiong, J., Cava, R. & Ong, N. Quantum oscillations and hall anomaly of surface states in the topological insulator Bi₂Te₃. *Science* **329**, 821–824 (2010).
- Peng, H. L. *et al.* Aharonov–Bohm interference in topological insulator nanoribbons. *Nature Mater.* **9**, 225–229 (2010).
- Xiu, F. X. *et al.* Manipulating surface states in topological insulator nanoribbons. *Nature Nanotech.* **6**, 216–221 (2011).
- Tian, M. L. *et al.* Dual evidence of surface Dirac states in thin cylindrical topological insulator Bi₂Te₃ nanowires. *Sci. Rep.* **3**, 1212 (2013).
- Dufouleur, J. *et al.* Quasiballistic transport of Dirac fermions in a Bi₂Se₃ nanowire. *Phys. Rev. Lett.* **110**, 186806 (2013).
- Gooth, J., Hamdou, B., Dorn, A., Zierold, R. & Nielsch, K. Resolving the Dirac cone on the surface of Bi₂Te₃ topological insulator nanowires by field-effect measurements. *Appl. Phys. Lett.* **104**, 243115 (2014).
- Guanhua, Z. *et al.* Growth of topological insulator Bi₂Se₃ thin films on SrTiO₃ with large tunability in chemical potential. *Adv. Funct. Mater.* **21**, 2351–2355 (2011).
- Tian, J. F. *et al.* Quantum and classical magnetoresistance in ambipolar topological insulator transistors with gate-tunable bulk and surface conduction. *Sci. Rep.* **4**, 4859 (2014).
- Bardarson, J. H., Brouwer, P. W. & Moore, J. E. Aharonov–Bohm oscillations in disordered topological insulator nanowires. *Phys. Rev. Lett.* **105**, 156803 (2010).
- Cook, A. & Franz, M. Majorana fermions in a topological–insulator nanowire proximity-coupled to an s-wave superconductor. *Phys. Rev. B* **84**, 201105 (2011).
- Cook, A. M., Vazifeh, M. M. & Franz, M. Stability of Majorana fermions in proximity-coupled topological insulator nanowires. *Phys. Rev. B* **86**, 155431 (2012).
- Rosenberg, G., Guo, H. M. & Franz, M. Wormhole effect in a strong topological insulator. *Phys. Rev. B* **82**, 041104 (2010).
- Zhang, Y. & Vishwanath, A. Anomalous Aharonov–Bohm conductance oscillations from topological insulator surface states. *Phys. Rev. Lett.* **105**, 206601 (2010).
- Ostrovsky, P. M., Gornyi, I. V. & Mirlin, A. D. Interaction-induced criticality in Z₂ topological insulators. *Phys. Rev. Lett.* **105**, 036803 (2010).
- Hong, S. S., Zhang, Y., Cha, J. J., Qi, X. L. & Cui, Y. One-dimensional helical transport in topological insulator nanowire interferometers. *Nano Lett.* **14**, 2815–2821 (2014).
- Cho, S. *et al.* Aharonov–Bohm oscillations in a quasi-ballistic three-dimensional topological insulator nanowire. *Nature Commun.* **6**, 7634 (2015).
- De Juan, F., Ilan, R. & Bardarson, J. H. Robust transport signatures of topological superconductivity in topological insulator nanowires. *Phys. Rev. Lett.* **113**, 107003 (2014).
- Ilan, R., Bardarson, J. H., Sim, H.-S. & Moore, J. E. Detecting perfect transmission in Josephson junctions on the surface of three dimensional topological insulators. *New J. Phys.* **16**, 053007 (2014).
- Jauregui, L. A., Pettes, M. T., Rokhinson, L. P., Shi, L. & Chen, Y. P. Gate tunable relativistic mass and Berry’s phase in topological insulator nanoribbon field effect devices. *Sci. Rep.* **5**, 8452 (2015).
- Chen, J. *et al.* Gate-voltage control of chemical potential and weak antilocalization in Bi₂Se₃. *Phys. Rev. Lett.* **105**, 176602 (2010).
- Hamdou, B., Gooth, J., Dorn, A., Pippel, E. & Nielsch, K. Aharonov–Bohm oscillations and weak antilocalization in topological insulator Sb₂Te₃ nanowires. *Appl. Phys. Lett.* **102**, 223110 (2013).
- Matsuo, S. *et al.* Weak antilocalization and conductance fluctuation in a submicrometer-sized wire of epitaxial Bi₂Se₃. *Phys. Rev. B* **85**, 075440 (2012).
- Ning, W. *et al.* One-dimensional weak antilocalization in single-crystal Bi₂Te₃ nanowires. *Sci. Rep.* **3**, 1564 (2013).
- Grbic, B. *et al.* Aharonov–Bohm oscillations in the presence of strong spin–orbit interactions. *Phys. Rev. Lett.* **99**, 176803 (2007).
- Yau, J. B., De Poortere, E. P. & Shayegan, M. Aharonov–Bohm oscillations with spin: evidence for Berry’s phase. *Phys. Rev. Lett.* **88**, 146801 (2002).
- Yang, M. J., Yang, C. H. & Lyanda-Geller, Y. B. Quantum beating in the conductance of ballistic rings. *Physica E* **22**, 304–307 (2004).
- Buttiker, M. Four-terminal phase-coherent conductance. *Phys. Rev. Lett.* **57**, 1761 (1986).
- Couto, N., Sacépé, B. & Morpurgo, A. Transport through graphene on SrTiO₃. *Phys. Rev. Lett.* **107**, 225501 (2011).
- Bardarson, J. H. & Moore, J. E. Quantum interference and Aharonov–Bohm oscillations in topological insulators. *Rep. Prog. Phys.* **76**, 056501 (2013).
- Gao, B., Chen, Y. F., Fuhrer, M. S., Glatli, D. C. & Bachtold, A. Four-point resistance of individual single-wall carbon nanotubes. *Phys. Rev. Lett.* **95**, 196802 (2005).
- Kobayashi, K., Aikawa, H., Katsumoto, S. & Iye, Y. Probe-configuration-dependent decoherence in an Aharonov–Bohm ring. *J. Phys. Soc. Jpn* **71**, 2094 (2002).
- Hansen, A. E., Kristensen, A., Pedersen, S., Sorensen, C. B. & Lindelof, P. E. Mesoscopic decoherence in Aharonov–Bohm rings. *Phys. Rev. B* **64**, 045327 (2001).
- Ferrier, M. *et al.* Geometrical dependence of decoherence by electronic interactions in a GaAs/GaAlAs square network. *Phys. Rev. Lett.* **100**, 146802 (2008).
- Ludwig, T. & Mirlin, A. D. Interaction-induced dephasing of Aharonov–Bohm oscillations. *Phys. Rev. B* **69**, 193306 (2004).
- Texier, C. & Montambaux, G. Dephasing due to electron–electron interaction in a diffusive ring. *Phys. Rev. B* **72**, 115327 (2005).
- Buchholz, S. S., Fischer, S. F., Kunze, U., Reuter, D. & Wieck, A. D. Nonlocal Aharonov–Bohm conductance oscillations in an asymmetric quantum ring. *Appl. Phys. Lett.* **94**, 022107 (2009).
- Yacoby, A., Schuster, R. & Heiblum, M. Phase rigidity and $h/2e$ oscillations in a single-ring Aharonov–Bohm experiment. *Phys. Rev. B* **53**, 9583 (1996).

Acknowledgements

TI material synthesis, characterization and part of the magneto-transport studies were supported by a DARPA MESO programme (grant no. N66001-11-1-4107). Part of the FET fabrication and characterizations were supported by Intel Corporation. The later stage of this work at Purdue was also supported in part by the National Science Foundation (DMR-1410942). L.A.J. acknowledges support by an Intel PhD fellowship and a Purdue Center for Topological Materials fellowship. L.P.R. was supported by the U.S. Department of Energy, Office of Science, Office of Basic Energy Sciences under Award Number DE-SC-0008630. Y.P.C. and L.A.J. thank M. Franz, J.H. Bardarson, T. Kubis and F.W. Chen for discussions.

Author contributions

L.A.J. designed and fabricated the devices and carried out the measurements and data analysis. M.T.P. and L.S. synthesized the Bi₂Te₃ nanoribbons and performed structural analysis. L.P.R. helped with the low-temperature transport experiment. Y.P.C. supervised the research. L.A.J. and Y.P.C. wrote the paper with contributions from all co-authors.

Additional information

Supplementary information is available in the [online version](#) of the paper. Reprints and permissions information is available online at www.nature.com/reprints. Correspondence and requests for materials should be addressed to Y.P.C.

Competing financial interests

The authors declare no competing financial interests.